Journal of Magnetic Resonance **138,** 144–154 (1999)
Article ID jmre.1998.1703, available online at http://www.idealibrary.com on IDEAL®

Practical Aspects of Birdcage Coils

F. David Doty, George Entzminger Jr., Cory D. Hauck, and John P. Staab

Doty Scientific, Inc., Columbia, South Carolina 29229

Received July 6, 1998; revised December 18, 1998

Numerical modeling and experimental results are presented for a variety of birdcages for high-field MRI microscopy. The data include the first published numerical calculations and experimental measurements of magnetic filling factors of birdcages or other MRI coils. Fast, 3D calculations for shielded coils are demonstrated using the Biot–Savart law along with energy minimization. It is shown that the near-field, higher-order inhomogeneity effects remaining after a first-order, asymmetry correction may easily exceed 20% in situations where it is desirable to maximize filling factor. It is also found that an order-of-magnitude improvement in the accuracy of predicted capacitor values may be achieved by using a more detailed circuit model of the birdcage resonator.

Key Words: coils; birdcage; filling factor; inhomogeneity; microscopy.

INTRODUCTION

For more than a decade, the birdcage coil has usually been chosen for magnetic resonance (MR) imaging (*1–4*) because of its ability to achieve circular polarization with high homogeneity under many conditions, but there are still a number of practical and theoretical issues that have not been fully addressed, especially for applications at high fields. It has been shown that the first-order quadrature and balancing errors in the birdcage can be corrected with just two judiciously placed capacitors (*4*). This has been quite effective in compensating for manufacturing tolerances in smaller coils at low fields, where sample-dependent shifts and asymmetries are small.

At higher fields with large and variable loads, the high-order homogeneity errors can apparently be addressed only by a very complex tuning procedure, as the parasitics cannot be precisely controlled. Moreover, these homogeneity errors in the near field of the conductor elements must be addressed in most microscopy applications (where filling factor is more important) and in whole-body MR, where space is critical. Otherwise, the birdcage's homogeneity in many situations (especially with asymmetric samples, noncylindrical coils, short coils, close shields, and double resonance) is far from what might be expected from standard theoretical treatments. While our starting point was microscopy, where resonator unloaded Q_0 and filling factor η_F are often as important as inhomogeneity σ, the nonideal factors in rf coil design are becoming more important for whole-body MR because of economic factors pushing toward smaller magnets. This implies, for example, that a perfectly tuned long elliptical birdcage with a small elliptical sample inside a magnet of unlimited diameter bears little practical relationship to most real-world applications.

The magnitude of B_1 homogeneity in the real birdcage may not be well appreciated by all users because most authors have calculated B_1 homogeneity only for several planes for a symmetrical sample, with perfect tuning, no ring currents, infinite rung length, and usually no external rf shield. Various groups have been performing 3D finite element analysis (FEA) of coils using subsets of Maxwell's equations or simplifying assumptions for the past decade—sometimes including the effects of the external rf shield on homogeneity in the absence of sample effects, tuning errors, and all losses (*5*). Recently, a more complete model has been reported showing effects of sample conductivity and permittivity (*6*), but this too included major assumptions: no input/output coupling loops, perfect tuning, long rungs, lossless conductors and capacitors, 2D symmetries, and a relatively small sample (62% of the coil diameter). Lest we give the impression that our treatment is intended to be complete, we should emphasize that we will retain long-wavelength assumptions and simplified loss models, but will no longer assume lossless circuits, perfect tuning, symmetrical coupling, and 2D symmetry.

We are aware of no prior calculations of magnetic filling factor (*7*) for any modern coil, even though improved filling factor is the indicated motivation for the development of many specialized coils, such as elliptical resonators (*8*) and capped head coils; and loaded and unloaded Q values have also not been previously predicted—even for a largely idealized birdcage. The reason for the limited prior treatments is that the math for real resonators is intractable and, notwithstanding many vendors' claims, fully suitable FEA software for rf coils has not been readily available. Two vendors (*9*) have recently released software for the NT platform possibly more capable of addressing these rf coil problems, which may make it feasible for us and others to extend the work we have done to date on these problems with rather limited software. A more accurate understanding of all losses (coil, sample, capacitor, shield, radiation) and filling factor is essential for further improvement in signal-to-noise ratio (SNR).

1090-7807/99 $30.00

B_1 HOMOGENEITY, FILLING FACTOR, AND Q VALUES

To simplify the data presentation and interpretation and to conserve space, we generally depart from the more common approach of showing contours of transverse field magnitude in several planes in favor of calculating the average variation σ in absolute value of the transverse B_1 component expressed as a percentage of mean B_1 throughout a specified sample volume (*6*), though alternative definitions have also been used (*5, 10*). Maximum deviation is often four to seven times σ, but the extremes are confined to small regions near the conductors. We typically evaluate σ from over 30,000 points on a Cartesian grid within the sample in coils that are symetric with respect to reflections about the $x = 0$, $y = 0$, and $z = 0$ planes.

The filling factor η_F is traditionally defined as the magnetic energy in the transverse component of the magnetic field throughout the sample divided by the total magnetic energy T throughout all space (recall $T = I^2L/2$ for a simple coil). However, in order for the concept to apply properly to circular polarization, it is better to define η_F in terms of the *rotating* component B_1:

$$\eta_F = \frac{\int_S B_1^2 dV}{2\mu_0 T}. \qquad [1]$$

For linear polarization, the filling factor is then one-half (not one-fourth, as mistakenly indicated in our earlier paper (*11*)) of the energy of the transverse component in the sample divided by the total energy. Some coil designers have suggested that the filling factor is not important when sample losses dominate, as loaded Q usually decreases almost as $1/\eta_F$. However, our experience suggests that η_F is more important than unloaded Q_0 from a design perspective, and focusing on η_F is often the best way to minimize sample losses.

A simple method for directly measuring the magnetic filling factor which makes it much easier to quantify rf coil efficiency has recently been described (*12*). If a small metal sphere of volume V_M is introduced into a homogeneous circular polarization sample region of volume V_S, the magnetic filling factor is given simply by

$$\eta_F \cong \frac{4f_\delta V_S}{3f_0 V_M}, \qquad [2]$$

where f_δ is the shift in resonant frequency f_0. The expression is accurate only when the test ball is in a uniform transverse magnetic field with low electric fields and negligible axial magnetic field. (With a saddle coil, for example, it may tend to overestimate B_1 near the window and underestimate it near the sidebands, even where electric and axial-magnetic fields are negligible.)

We define a dimensionless coil field factor β that permits simple calculations of B_1 when scaling coils (*11*):

$$\beta = \sqrt{20\eta_F V_C / V_S}. \qquad [3]$$

Then,

$$B_1 = \beta\left[\frac{\eta_E P Q_L}{f_0 V_C}\right]^{1/2} \quad \text{[mixed units]}, \qquad [4]$$

where η_E is the rf circuit efficiency (the fraction of rf power delivered to the coil, its capacitors, and sample—nearly unity for many fixed-frequency circuits), P is the transmitter rf power in watts, f_0 is the frequency in megahertz, and V_C is coil volume (here, it is in milliliters). For example, β equals 3.16 for the infinite solenoid, about 1.4 for the typical slotted resonator when coil volume is based on window height, about 3.1 for the ideal birdcage, and about 1 to 2 for the typical birdcage.

Loaded Q_L may be calculated with reasonable accuracy when electric fields from the coil are minimal (which in principle is usually possible) by first estimating a limiting sample Q_S from inductive losses (*11*),

$$Q_S \cong \frac{32\pi\rho_S \xi V_C}{\mu_0 \eta_E \beta^2 \omega V_S^2}, \qquad [5]$$

where ρ_S is the electrical conductivity of the sample, ξ is the flux path length (mean distance along the B_1 direction) through the sample, and V_S is the sample volume. Equation [5] can be shown to be in agreement with an earlier one derived by Carlson (*3*) for a spherical sample and a more recent, general calculation by Macovski (*13*). Q_L is then calculated from

$$\frac{1}{Q_L} = \frac{1}{Q_{0L}} + \frac{1}{Q_C} + \frac{1}{Q_S} + \frac{1}{Q_R}, \qquad [6]$$

where Q_{0L} is the effective Q of the inductors, Q_C is the weighted mean Q of the capacitors, and Q_R is the radiation-resistance Q limit. The resonator Q_0 is the parallel combination of Q_{0L} and Q_C. A leading manufacturer gives Q data for their highest quality UHF 1KV multilayer ceramic chip capacitors that approximately fit the following equation for the range 30–800 MHz for capacitors in the range of 5–100 pF,

$$Q_C \approx 1.7E07 C_P^{-0.75} f_0^{-1.45}, \qquad [7]$$

where C_P is the capacitor value (in pF). For example, a 15-pF capacitor at 120 MHz may have $Q_C = 2200$, while a 20-pF capacitor at 300 MHz is likely to have $Q_C = 460$. Thus, in high-field MR coils (contrary to VHF radio) Q_{0L} and Q_C are usually comparable. (Of course, it is sometimes practical to use

copper-clad Teflon, quartz, or alumina capacitors and achieve two to eight times higher Q_C. This has formed the basis of most of the progress in NMR probe *S/N* in the past several years.)

Radiation resistance (which generally increases as ω^4) quickly becomes more significant than either capacitor or inductor losses in large coils when the distance from the coil to the shield is an appreciable fraction of a wavelength, but we will not address the Q_R term here.

While Q_0/Q_L is often used as an indicator of coil quality (*14*), sample loading degrades Q_L by at least two mechanisms that do not contribute to signal: currents induced by axial rf magnetic fields and electric fields from self-inductance of the coil. Hence, we find the classic NMR *S/N* dependence $(\eta_F Q_L)^{1/2}$ to be the best dimensionless figure of merit when voxel size is a constant fraction of sample size.

A number of dimensioned figures of merit are also in use, including $(\tau_{90}\sqrt{P})^{-1}$ and $B_1/\sqrt{I^2R}$. But I and R are seldom independently determined, so $B_1/\sqrt{P}$ (which, from Eq. [4], equals $\beta(\eta_E Q_L/V_C)^{1/2}$ within a proportionality constant) is more direct. Perhaps the most widely used (inverse) performance figure is τ_{90} (the $\pi/2$ pulse length with a square pulse) at a specified power, which is readily shown from Eq. [4] and basic NMR principles to be

$$\tau_{90} = \frac{\pi}{2\gamma\beta}\left[\frac{f_0 V_C}{\eta_E P Q_L}\right]^{1/2}. \qquad [8]$$

THE CURRENT DENSITY PROBLEM IN RF COILS

It has been well known for at least five decades that the current does *not* distribute itself uniformly over the surface of any real coil to a nominal depth given by the classical skin depth of an infinite plane wave near the surface of a planar conductor, and there were early attempts to quantify the surface current distribution in terms of a proximity factor for certain coils. While a general, analytical solution is probably impossible, software may be becoming available that is capable of providing *approximate* numerical solutions.

An elegant and efficient partial 2D solution for *axially oriented* conductors based on inverse Hilbert transforms presented by Crozier *et al.* (*15*) appears to give current distributions across rungs roughly in agreement with our estimates for the high-Q case, though it does not appear that they considered thickness effects at the foil edges or resistance in the conductors (they assume that **E** has no z component), which we often find to be significant. Our numerical modeling suggests that edge current densities in foil rungs are typically about a factor of 5 above mid-rung values (rather than singularities at the edges). We find mean rf flux penetration to be about six times the classical skin depth δ at the edges of conductor foils that are 6δ thick in typical rf coils, and this does not appear to be an artifact of conductor defects near the edge, as it is not significantly affected by electropolishing or annealing. These edge effects are less significant with very thick conductors, but thick conductors (especially if the birdcage is segmented by capacitors anywhere except in the end rings) often are the source of excessive $\mathbf{B}_0$ inhomogeneities (*16*), and thick guard rings may contribute to gradient eddy current problems (*17*).

Certain aspects of the detailed current distribution can be understood in general terms. While the DC distribution minimizes power dissipation, the rf current distributes itself so as to minimize stored energy—i.e., minimum inductance—when the coil Q is infinitely high. The typical rf solution lies somewhere in between. The computational difficulty of this problem may be appreciated by noting that the element size for a conventional FEA approach must be about a micrometer (a fraction of the classical skin depth) near critical surfaces in portions of the conductors, but the rf fields often extend over tens or hundreds of millimeters. Even for a small coil (10 mm diameter) with a highly sophisticated meshing algorithm, the complete 3D FEA solution requires a minimum of several million elements, which is an order of magnitude beyond practical computational limits. However, not having a complete software solution does not prevent us from determining with reasonable accuracy the macroscopic current distributions for any high-Q coil—it simply means that we cannot accurately predict Q_{0L}.

An augmented Biot–Savart approach has the capability of quickly solving most rf coil problems with arbitrarily oriented conductors in the absence of dielectrics for long wavelengths. The current distributions are not initially known and must be determined in an iterative fashion that can be extremely time consuming with commercial software. For this reason, we developed our own software (in C++ for Windows 95), dubbed *COILS,* to be particularly well suited to manipulations of typical surface current distributions. Our recalculations on a 300-MHz Pentium-II typically take a few seconds to a few minutes, depending on the extent of the changes and the mesh sizes. A major part of the problem has been automated. For example, a simplex algorithm determines the external shield currents such that the external field is minimized, but current distributions across coil conductor elements in the coil are often determined in a semimanual method by requiring perpendicular components of $\mathbf{B}_1$ to vanish near the surface of wide conductors or by minimizing inductance while holding total current constant. A high level of confidence in this approach has been established from 5 years of experience in successfully applying *COILS* to numerous gradient, susceptibility, and coil problems, as described in more detail elsewhere (*16, 17*).

Filling factors and inductance can easily be calculated exactly for several infinitely long geometries—for example, the solenoid, coaxial resonator, and the immersed, shielded, slotted resonator (in all these cases, $\eta_F = 0.5$). Analytical approximations for very long versions of these resonators agreed with values obtained from *COILS* within ~2%.

The main reasons for wanting to know detailed current distributions are (a) to develop novel coil geometries that achieve high B_1 homogeneity without relying on precision

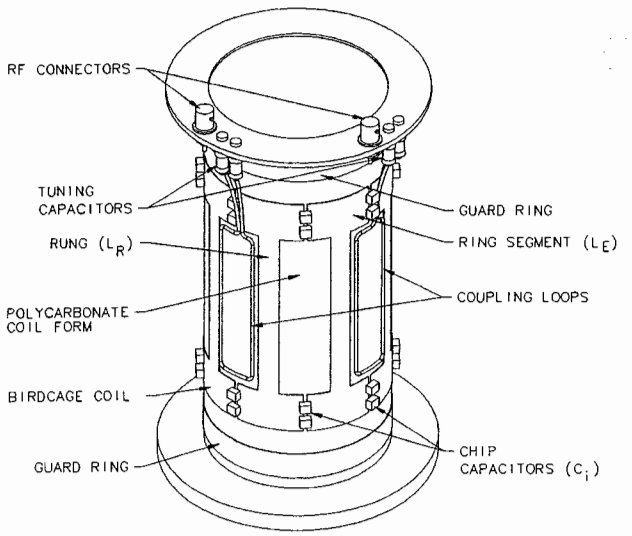

FIG. 1. 3D rendering of a typical birdcage.

tuning and balancing and (b) to optimize sensitivity—i.e., $\eta_F Q_L$. At present, macroscopically accurate current distributions for us means reasonable accuracy in current gradients over distances of about 2% of the coil diameter, which appears adequate for optimization of coil geometries for frequency–diameter (fd) products greater than 10 MHz-m, where Q_{0L} is often larger than Q_C, and Q_S normally dominates.

The obvious dimensional proportions of the birdcage shown in Fig. 1 may explain why the effects of the ring currents have often been ignored—the ring segments are normally very short compared to the rungs. What is not obvious without a more detailed approach is the extent to which these currents are concentrated on the inside edges of the rings. These concentrations are more detrimental to η_F and Q_L than has generally been appreciated.

EXPERIMENTAL AND NUMERICAL RESULTS FOR PRECISELY TUNED CYLINDRICAL BIRDCAGES

Table 1 shows measured and calculated data (Q_0, Q_L, η_F, and B_1 inhomogeneity σ) for a number of birdcages. We list both overall coil length and rung length for more direct comparisons to novel coils which will be presented in a subsequent paper. The frequency is 200 MHz; the coils are fabricated from 0.06-mm copper foil (~10 skin depths) on kapton and mounted on the outside of a polycarbonate coilform; guard rings, equal in width to the ring width, are mounted inside the coilform, which is 3 mm thick; the sample is an asymmetric, saline load comparable to the largest live animal that will fit in the coil (35 mM, or 0.4 S/m); the rf shield is a long, continuous, cylindrical copper shell; relative rung width is also equal to the central surface coverage ratio (fraction of surface covered by foil); ring width is approximately twice rung width, and two or three well-spaced paralleled chip capacitors (of sum C_i) are used at each node to reduce parasitic effects. The coils typify microscopy and *in vivo* coils where Q_{0L} and η_F are still quite important. The effects of the sample (in a thin plastic container) are shown by Q_L and f_{DT}—the percentage change in resonant frequency when the sample is inserted.

An important point is that, for the cylindrical samples, Q_L and f_{DT} are measured with a *long,* asymmetrically placed, cylindrical sample extending from one end of the homogeneous region to at least a full coil radius beyond the other end of the homogeneous region, as this more closely approximates

TABLE 1
Well-Tuned Balanced-High-Pass Quadrature Birdcages at 200 MHz

Expt No.	O.A. length (mm)	Rung length (mm)	Sample ROI diam (× length) mm (× mm)	Shield diam (mm)	No. of rungs	C_i (pF) Meas.	Q_0 Meas.	Q_L Meas.	η_F (%) Calc.	η_F (%) Meas.	f_{DT} (%) Meas.	σ (%) Calc.
1	173	150	Sphere, 70	200	16	16	319	87	5.5	4.8	0.98	0.5
2	131	109	Sphere, 70	200	16	20	224	82	6.9	6.1	1.54	2.5
3	131	109	80 × 80	200	16	19	224	11	14.0	13.6	4.89	4.6
4	136	105	80 × 80	200	12	14	268	13	14.6	13.2	4.63	5
5	136	105	80 × 80	140	12	18.6	237	17	9.4	8.7	5.58	6
6	146	99	80 × 80	140	8	12	296	26	9.6	7.9	2.30	9.5
7	140	110	78 × 78	140	8[a]	10	182	30	8.1	6.8	5.75	8.2
8	131	109	80 × 80	120	16	44	327	52	5.6	5.3	1.74	5.7
9	146	99	80 × 80	120	8	19	165	29	5.4	4.4	2.89	13
10	147	69	80 × 60	120	8[a]	28.5	349	51	6.0	5.5	3.21	12
11	107	75	Sphere, 70	140	12	27	355	97	5.5	5.2	0.75	6
12	107	75	80 × 50	140	12	26	355	26	7.4	5.8	3.36	8
13	39	22	Sphere, 30	100	8	49	249	187	11.4	8.7	0.3	12
14	39	22	32 × 16	50	8	86	200	156	4.7	4.2	0.25	15

[a] Relative rung width is ~0.3 except as follows: it is 0.2 in experiment 7, and 0.5 in experiment 10. The last two coils are 40 mm in diameter, while the rest are 100 mm. Sample effects on σ are ignored.

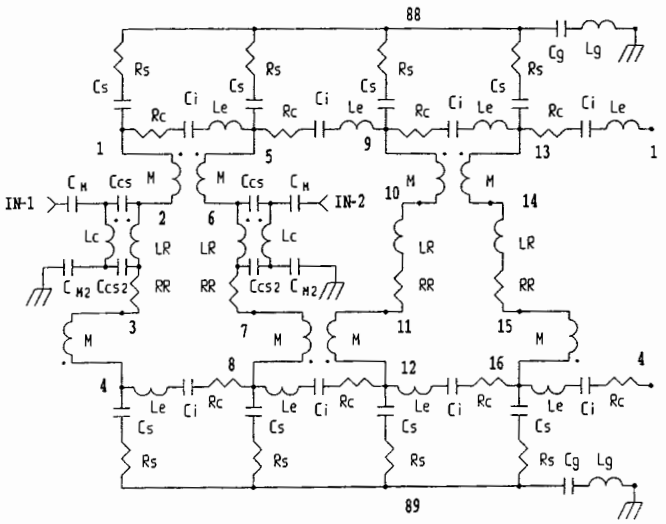

FIG. 2. RF circuit model of the four-rung balanced-high-pass birdcage with major parasitics.

most applications and is more difficult to deal with than, for example, a sample of half the volume and four times the salinity. The Q data are averages of several measurements with different coupling loops using a calibrated reflectance method as previously described (*18*) and normally agree within 10% with various other methods.

We limit this evaluation to midsized, balanced-high-pass birdcages (BHP-BC), although similar conclusions apply to others of comparable *fd* product (8 to 20 MHz-m, typical for mice at 500 MHz, rats at 300 MHz, human head at 80 MHz, etc.), whether high-pass or bandpass (hybrid), although the latter would probably not be chosen for these applications. (Note that the BHP-BC is often simply called the "high-pass" birdcage, but this also often refers to the unbalanced or single-ended design.) We emphasize that while rung errors may be as small as several percent in the laboratory, rung errors to 15% should be expected in many real-world situations. For example, moving the sample near one side may produce a large capacitive error on one or two rungs, or placing the coil off center inside the rf shield may cause an inductive error of this magnitude in several rungs.

Tropp considered small rung errors (<4%) in his elegant first-order theoretical analysis and concluded that they could easily be corrected without knowing their actual location and value with two properly positioned corrections (*19*), and he recently extended the theory to include mutual inductances in unbalanced birdcages (*20*). A more complete solution, made possible only with standard, linear-circuit-analysis software (*21*), permits a more detailed near-field picture and one that agrees with our experience.

The rf circuit model we used for the BHP birdcage is shown schematically in Fig. 2 for the four-rung case for brevity (some of the nodes are numbered), with obvious extension to higher orders. Note that the major parasitics are shown. These include (roughly in typical order of importance) (a) sample losses R_S (200–2000 Ω); (b) input coupling balance (C_M, C_{M2}, C_{CS}, and C_{CS2}); (c) stray capacitance C_S to the guard rings (3–5 pF), shield, and sample (1–3 pF); (d) reactance from the guard rings to ground (C_G, L_G); (e) mutual inductance M to adjacent rungs; (f) series resistance R_C (from Q_C) of the tuning capacitors; (g) series inductance L_E of the ring and capacitor leads; and (h) series resistance R_R of the rungs. The values of C_S and R_S were somewhat larger at one end than at the other end because of the asymmetrically placed sample. It should be pointed out that while C_G and L_G have no effect when the birdcage is perfectly symmetrical, small asymmetries (in stray capacitances C_{CS} and C_S, for example) often make them responsible for extremely troublesome parasitic resonances. Representing stray capacitance at each node as two parallel C_S's, one of low loss (to the guard ring) and one in series with R_S, simplifies some of the parameter fitting.

The quadrature inputs are inductively coupled into two orthogonal locations as usual, and their effects on symmetry are found to be substantial for loaded coils. Asymmetric stray capacitive coupling (C_{CS}, C_{CS2}) to the inductive coupling loops is often one of the most significant perturbations. It may be partially addressed with ganged match/balance variable capacitors (C_M, C_{M2}), but this is seldom satisfactory from an operations perspective.

Even more severe problems may arise from balanced transmission lines between the ring nodes and fine-tuning capacitors when it is not possible to place them directly on the rings in parallel with C_i. The rung inductors L_R were later replaced with sections of transmission lines to more accurately include the effects of distributed capacitance and propagation delays, but the lumped model was quite adequate for *fd* products at least up to 25 MHz-m. One difficulty with the model is its need for empirically determined reductions in L_R (from flux exclusion by the sample) and decreases in R_S as sample salinity increases.

The rf software only allows calculation of currents, voltages, phases, impedances, and couplings throughout the circuit as a function of frequency from assumed values for the various circuit elements. To determine the field throughout space, the calculated loop currents are then fed into *COILS*. In the circuit modeling, inductors and capacitors are given appropriate Q's (300 to 1500), and propagation effects are ignored in our magnetic field calculations. Jin and Chen have recently shown that (ignoring the electric field effects of capacitive segmentation and the self-inductance of the coil) dielectric and conductivity effects within the human head perturb B_1 homogeneity in the central plane in a perfectly tuned coil by about 4% for *fd* ≅16 MHz-m with the sample diameter 62% of d, and the perturbation increases approximately linearly with *fd* (*6*). While not directly reported, it appears from their work that σ over a typical biological sample volume at this *fd* may be about 10% for a large, perfectly tuned, 16-rung birdcage.

Ring currents have usually been omitted in the calculation of

B_1 inhomogeneity for circular polarization, but their transverse fields are coherent with those of the rungs and thus do not average to zero over a complete cycle for a rotating field. We performed the calculations both with and without the ring currents and were surprised to find that the presence of the ring currents generally improves σ, both for spherical and for cylindrical samples. Like prior works, the inhomogeneity calculations in Table 1 ignore the effects of input couplings. Sample permittivity and conductivity effects are also ignored in the calculation of σ. The filling factor calculation integrates the square of the field and thus must also include the ring currents. The η_F listed in Table 1 is for circular polarization; for linear polarization, divide by 2. Measurement accuracy for η_F was typically limited to $\sim\pm 0.006$ (i.e., $\sim 10\%$ accuracy for a filling factor of 6%), as the volume of the metal test probe was $\sim 7\%$ of the sample volume and $Q_0 \sim 250$. Coil volume is defined using overall coil length.

Experiment 1, Table 1, establishes a reference point to theoretical treatments based on 16 long rungs and a midsized, spherical sample. While homogeneity is very high as expected ($\sigma = 0.5\%$), the filling factor is only $\sim 5\%$, even though the shield/coil diameter ratio is 2. In row 2, we see the somewhat improved filling factor from a shorter coil ($\eta_F \sim 7\%$), but σ has increased to 2.5%.

Experiment 3 shows the degradation in σ but improved η_F that occurs for a large cylindrical sample, which often more closely approximates the ROI (region of interest, or at least the acceptance test phantom and the sensitive region of the coil) than does the sphere. Note that η_F is still only 14% and sample detuning f_{DT} (nearly 5%) has become a serious problem, as this tuning shift is three times the tuning range of the coil before its B_1 homogeneity is severely spoiled (i.e., σ is increased by about a factor of 5). (Further segmentation, as in the balanced-bandpass birdcage, could reduce the detuning, but the tuning range is reduced even more and it also increases tuning complexity.)

Next, in experiment 4, we show that reducing the number of rungs to 12 (which makes tune-up more practical and helps Q_0 in smaller coils by improving Q_C) has no significant effect on η_F or σ when the shield diameter is large but sometimes helps both Q_0 and Q_L. In line 5, we reduce the shield diameter to $1.4d$, which still has little effect on σ, but hurts η_F as expected. In experiment 6 we reduce the number of rungs to eight, at which point the difference between rung-feeding and inter-rung feeding becomes significant (*15*). We show results for the better case—inter-rung feeding—but still find $\sigma = 9.5\%$ for perfect tuning and no loading. In line 7, the rung widths and sample dimensions are reduced to establish a reference point to a previously published coil design of similar fd product and similar dimensional ratios for validation—coil 1 by Crozier *et al.* (*15*), with inter-rung feed, for which they calculated relative rms deviation of 8.9% without including ring and external shield currents (we calculate 11.5% relative rms deviation including these effects).

In experiment 8 the shield diameter is further reduced to $1.2d$ and the number of rungs increased to 16—typical for larger, *in vivo* coils, where the magnetic filling factor is under 6% even though the volumetric filling factor is near 50%.

In experiment 9, we return to the more typical high-field microscopy coil in a vertical bore magnet, where 8 rungs is usually the practical limit. The closely spaced shield severely degrades B_1 homogeneity ($\sigma = 13\%$) and this also tends to degrade Q_L, though the degradation in dropping from 16 to 8 rungs may be negligible when the sample diameter is under 65% of the coil diameter (*6*). However, relative SNR is down by only $\sim 25\%$ compared to experiment 4, as the factor of 3 drop in η_F is partially offset by an increase in Q_L, as expected. Reducing the coil length helps SNR for short samples, especially if relative rung width is increased, as this helps both Q and η_F, as shown in experiment 10. However, the actual performance of small, low-inductance resonators, as in experiments 8 and 10–14, depends strongly on capacitor Q's, as their losses are comparable to the inductor losses, which explains prior observations of Q_0 decreasing with increasing number of rungs in small, high-pass resonators. In experiments 11 and 12, very short birdcages are tested, and in 13 and 14 we reduce the coil diameter to 40 mm to show Q dependencies.

The first quadrant of the B_1 field vector projection in the $x = 0$ plane for B_1 phase at 90° for simulation 10 is illustrated graphically in Fig. 3 to provide some insight into both the intensity and the direction of B_1 in regions that contribute strongly to reducing the filling factor. The coil (foil) conductor sections are represented by the closely spaced small circles at a radius of 50 mm. Note that a much greater end ring width (from $z = 40$ to 70) than normal was used to minimize unusable magnetic energy in this region, and a portion of the coupling loop is visible at $z = 50$, $r = 53$ mm. Currents induced in the external shield (at $r = 60$ mm) are also represented by small circles. The field vectors are represented by directed segments of length proportional to the projected magnitude. (Energy density is proportional to the square of the segment lengths. A coarse grid is used here for improved graphic clarity.)

The significance of the parasitics and standard model approximations even in symmetrical, cylindrical birdcages of moderate difficulty may be partially appreciated by noting that the capacitor values predicted by a publicly available program based on published methods of calculating self- and mutual inductances for shielded (balanced) high-pass birdcages (*22*) differ from the experimental values by amounts ranging from -20 to $+50\%$ for the first 12 birdcages listed in Table 1, where in all cases $fd = 20$ MHz-m. On the other hand, once the major parasitics have been determined by fitting them to experiments at both a low and a high test frequency for a given coil geometry, the circuit model of Fig. 2 predicts tuning capacitor values within 3% over the frequency range of 50 to 250 MHz. However, the severely limited tuning range of the birdcage makes even this accuracy insufficient to com-

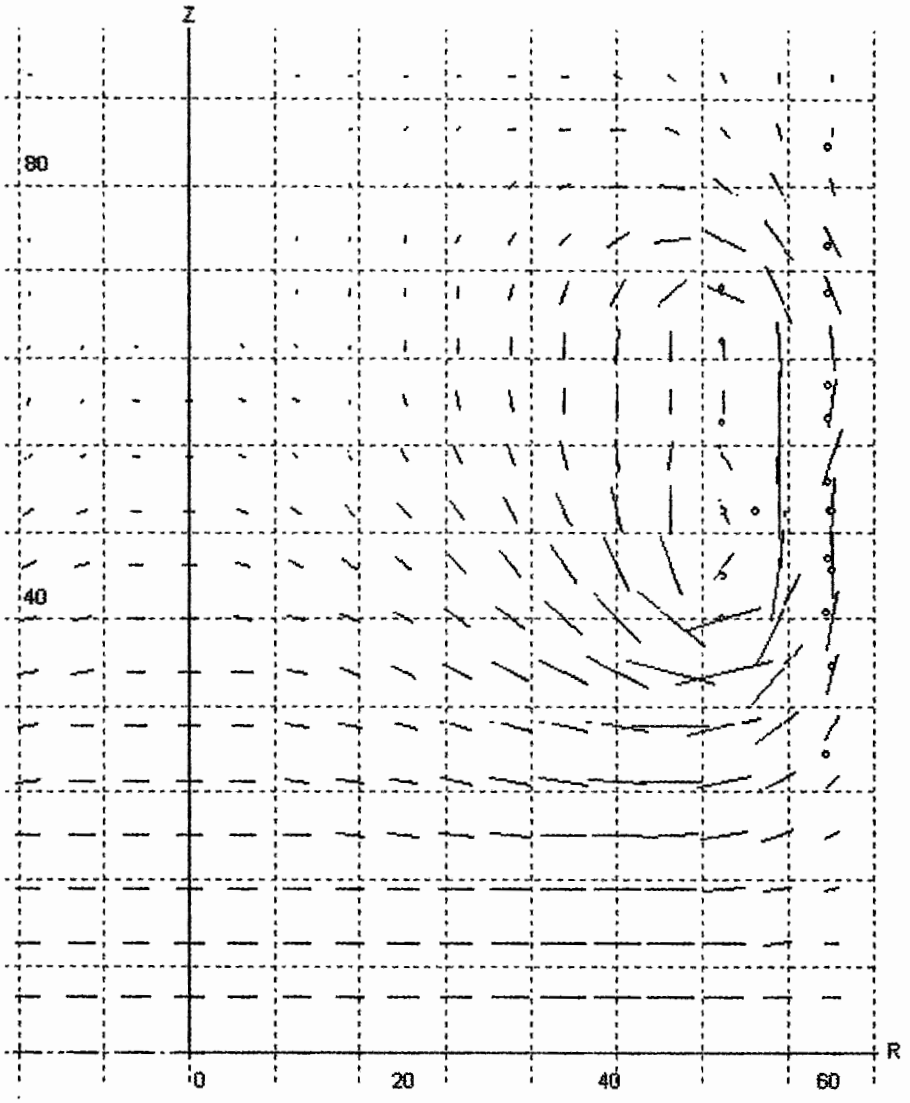

FIG. 3. Field magnitude and direction for the $x = 0$ plane for experiment 10.

pletely eliminate trial and error in many cases. Semiempirical methods of estimating the major parasitics based on various details of the coil and sample geometry could be developed to reduce the amount of trial and error in building high-field birdcages.

It appears that less than 25% of the mean discrepancy (~14%) between our calculated and measured filling factors can be explained by inductance of the chip capacitors (which was ignored in the *COILS* model) and electric field interactions with the measurement test ball. The approximations used in the Biot–Savart equation very near the current elements and current path approximations are probably more significant. Yet more important, in the first 14 simulations, all effects of the input coupling loops were ignored; and, to simplify descriptive detail, their effects on filling factor were also omitted in the asymmetric simulations of the following section. Also, the measured value of η_F is based on a single measurement of B_1 near the center, but the ratio of the calculated central value to the calculated mean value throughout the sample (which ranged from 0.98 to 1.02) was used to improve the accuracy of Eq. [2]. Considering the simple Cartesian meshing method, the agreement is quite close in most cases, and it suggests that rough estimates of η_F (*23*) that are not based on detailed calculations may be off by an order of magnitude.

FIG. 4. Field intensity for the $z = 0$ plane for the asymmetric birdcage of experiment 18.
FIG. 5. Field intensity for the $z = 0$ plane for the asymmetric birdcage of experiment 19.

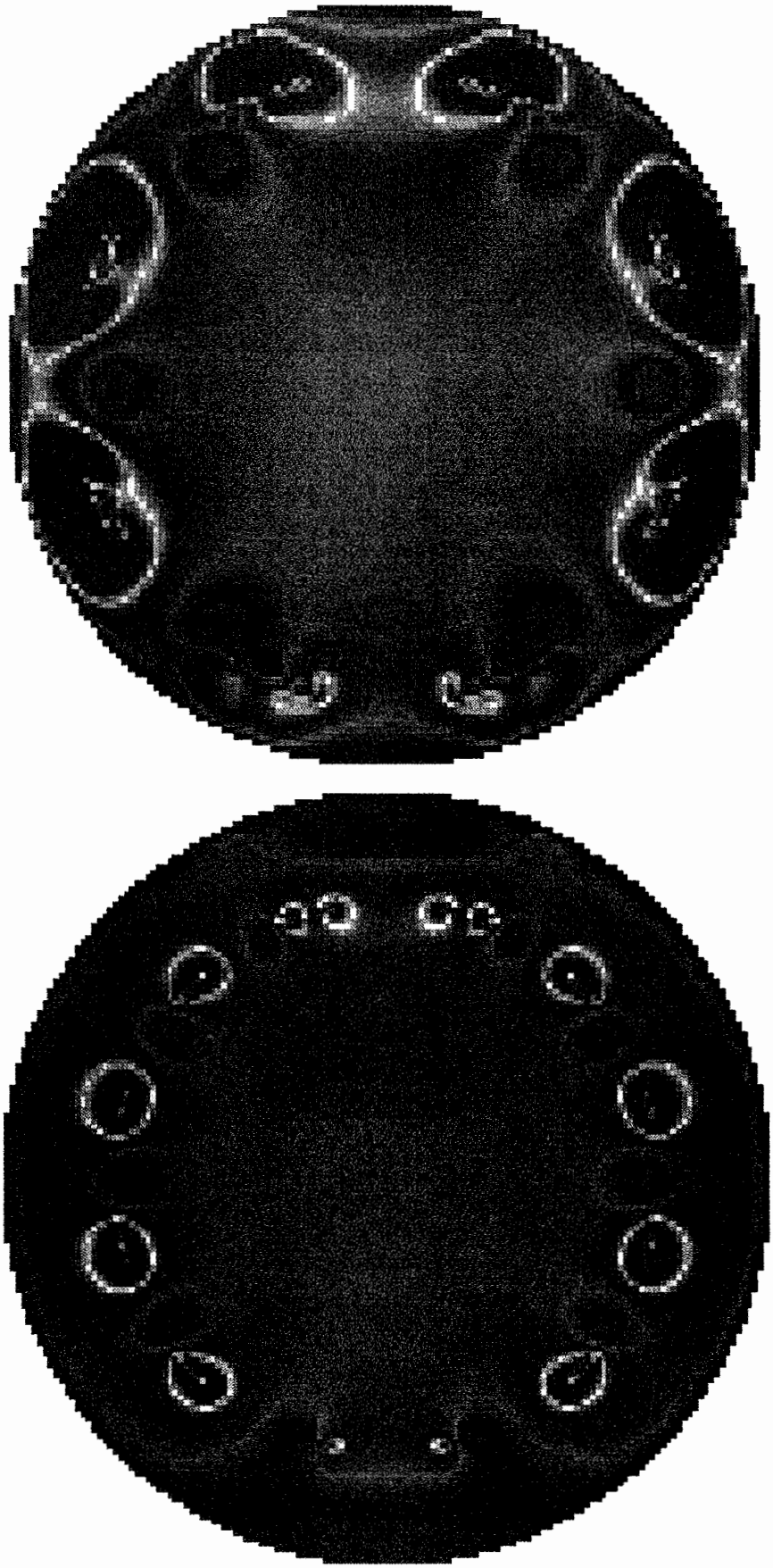

TABLE 2
Loaded, Matched, BHP 100-mm 200-MHz Birdcages

Expt No.	Expt No. from Table 1	Shield diam (mm)	No. of rungs	Sample length (mm)	Rung errors ±%	Current errors ±%	σ (%) Calc.	Rel. SNR, $(\eta_F Q_L)^{1/2}$ Meas.	τ_{90}, μs at 1 kW
15	5	140	12	80	2	10	9.1	12.2	97
16	7	140	8	80	4	20	10.3	14.4	79
17	8	120	16	80	5	25	12	16.5	71
18	10	120	8	60	4	20	14.1	16.8	61
19	12	140	12	50	2	10	11.6	12.3	76

Note. Data are for circular polarization.

EXPERIMENTAL AND NUMERICAL RESULTS FOR ASYMMETRIC BIRDCAGES

Several of the precisely tuned coils from Table 1 were detuned by increasing the capacitance (discrete plus stray) at one node by 2 to 5% and decreasing that at another node by a comparable amount. (While the BHP birdcage is less sensitive to sample dielectric loading than is the balanced-low-pass birdcage, an asymmetric sample can easily induce rung errors greater than this, especially as the *fd* product increases.) The orthogonal modes were both retuned to 200 MHz with isolation greater than 16 dB by corresponding changes in two capacitors 45° apart at fixed locations. The linear circuit model confirmed our expectations: especially as the stray capacitance becomes an appreciable fraction of the lumped capacitance, the current errors are often large compared to the capacitance errors and cannot be corrected without the ability to properly position the corrections. The calculated currents were entered into *COILS* to determine numerically the effects of these residual rung current errors on σ.

We were more surprised to discover the magnitude of the effect of symmetric resistive losses in an otherwise largely ideal birdcage. It has previously been suggested that symmetric losses (whether sample, coil, capacitors, shield) cannot affect B_1 homogeneity (*6*), but those arguments ignored the input coupling problem. The more complete rf model shows that for a Q_L of 25 with perfectly symmetric loading and typical input coupling methods, peak rung current errors of ±7% are induced. Moreover, these errors, being dipolar, have a greater effect on σ than the higher-order field of comparable, random rung errors. The calculated values for σ in Table 1 ignored the sample loading and input coupling effects. The practical effects are seen by comparing σ in Table 1 for a precisely tuned coil to σ in Table 2 for a similar coil which includes minimal effects of the quadrature input matching circuit (with large coupling loops) and two small rung errors of the listed magnitude. We still ignore sample rf penetration effects, which may add 5 to 10 percentage points to σ (*6*). If the sample diameter were reduced by 5% or shortened by 15%, the σ values would typically be 15% smaller than shown. However, there are many possibilities for the coupling method and locations of the tuning errors that result in much more degradation than listed for the large sample.

Figure 4 shows a color scale representation of the transverse magnitude of B_1 for the $z = 0$ plane for simulation 18 under linear polarization, and similar results for experiment 19 are shown in Fig. 5. In both cases, the homogeneity at the center is not seriously affected by either the coupling field or the error currents, but the increased inhomogeneities near the coupling loops (top of figures) are quite obvious. Circular polarization does relatively little to improve homogeneity, as the hot spots remain near the coupling loops.

The model and experimental results suggest that tedious, sample-dependent, fine tuning of the birdcage is needed to obtain high B_1 homogeneity for large samples with a closely spaced external shield. We were somewhat surprised by the magnitude of the local effect of tuning errors. Indeed, two trimmer capacitors at 45° spacing are sufficient to return the two modes to the same frequency, and the voltage/current distribution around the birdcage is roughly sinusoidal in both modes. However, our experiments and modeling show that 4% tuning errors in just 2 of the 16 capacitors C_i in an eight-rung BHP-BC produce rung current errors of ±12 to ±25% even when both modes are precisely tuned and matched to the same frequency! (The effect on σ is less than might be expected because σ is an average deviation over the full sample volume and the errors from one or two rungs are rather short ranged.) The sensitive tuning behavior indicated by our model does not appear to be exacerbated from the presence of axially asymmetric parasitics or inclusion of the input couplings.

When the mean frequency shift was small, four additional trimmer capacitors were often found to be sufficient to achieve impedance matching and precise orthogonality at the desired frequency, as indicated by >25 dB of isolation between the two ports, which is generally effective in reducing rung current errors to ±7%. However, at least four more trimmers are needed for these objectives when the sample detuning shift exceeds about 1.5% in the 8-rung microscopy birdcage, and 14 adjustments are often required to accurately correct and match a 3% mean shift in a 12-rung birdcage. The magnitude of the

asymmetry may be reduced by typically a factor of 4 through the use of baluns and twice as many coupling loops (two per phase, one on each side of the birdcage), but this sometimes leads to more false modes near the homogeneous resonance. The problem worsens as the number of rungs increases, especially with noncircular birdcages.

Our detailed modeling of the cylindrical birdcage leads us to believe that it will be essential to develop accurate methods of predicting parasitics for each rung in noncylindrical birdcage resonators before such coils are likely to be practical for most purposes. The initial mode splitting of 15% recently reported for a 16-rung elliptical birdcage using capacitors of 2% tolerance (*8*) appears consistent with expectations based on our cylindrical circuit model adapted to the elliptical case without correcting the parasitics. While inclusion of the end ring mutual inductances greatly improves accuracy (*24*), only the cylindrical geometry permits a simple, empirical determination of the stray rung capacitances, which have a huge effect on homogeneity. Some published results for elliptical birdcages show good homogeneity only for 25% of the central cross-sectional area, which suggests perhaps a factor of 2 reduction in filling factor compared to the cylindrical birdcage (even for somewhat elliptical samples), where high homogeneity may be achieved over at least 65% of the cross-sectional area. We have shown that further improvements in $(\eta_F Q_L)^{1/2}$ are possible with a more optimally chosen rung width.

Double-resonance birdcage resonators (*25*), where rung errors and stray capacitances can easily be four times greater, are also not practical in most settings at high fields, and efficient multinuclear tuning of birdcages appears out of the question. However, inhomogeneities three to five times larger than obtained for large samples in birdcages are generally unavoidable in phased arrays, and effective methods have been developed for dealing with them under many conditions (*26*).

CONCLUDING REMARKS

In the highly loaded birdcage, the effects of the input coupling loops on homogeneity are substantial, especially if they are not carefully balanced and if one is relying on just two variable capacitors for asymmetry correction. Tuning frequency shifts from variable, symmetric loads often exceed the practical tuning range of a birdcage by a factor of 3. Moreover, perturbations from asymmetric loads or hardware in high-field birdcages may exceed the effective range of a first-order correction by an order of magnitude.

The experimental and numerical results suggest that optimum relative rung width, both for best SNR and best homogeneity, is considerably greater than what is commonly seen in the literature and in general practice. In fact, it appears that increasing relative rung width from 0.2 to ~0.4 (or larger, for closely spaced shields) and optimizing diameter and length for the region of interest would often offer greater potential for improved performance than changing from a cylindrical to an elliptical birdcage, especially since detailed methods of estimating rung-dependent stray capacitance have not been reported for the elliptical resonator.

A recent calculation of ultimate achievable SNR concluded that a commercial 1.5-T MR body birdcage coil (mean $fd \sim 30$ MHz-m) obtained only 36% of theoretical limits near the very center and less than 10% of ultimate intrinsic SNR over most of the central region (*27*). Moreover, SNR relative to theoretical limits for smaller birdcages is often worse. We believe that detailed numerical optimizations of novel rf coil designs that focus on maximizing $(\eta_F Q_L)^{1/2}$ while minimizing σ are the most effective route to improved MRI coil performance. Novel coils that address some of the practical problems associated with the conventional, high-field birdcage are described elsewhere (*28*) and will be discussed in more detail in a subsequent paper.

ACKNOWLEDGMENTS

The authors thank numerous technicians and engineers at (or formerly at) Doty Scientific, especially Xunming Chen, Andy Yang, Eugene Deyneka, Glenn Doty, David McCree, Jiong Shao, Art Boman, and Mark Moore, for their assistance in programming, experiments, calculations, analysis, and prototyping. The authors also thank the referees for a number of helpful comments. This work was supported by Doty Scientific, Inc.

REFERENCES

1. C. E. Hayes, W. A. Edelstein, J. F. Schenck, O. M. Mueller, and M. Eash, An efficient highly homogeneous radiofrequency coil for whole-body NMR imaging at 1.5 T, *J. Magn. Reson.* **63,** 622–628 (1985).
2. W. A. Edelstein, J. F. Schenck, O. M. Mueller, and C. E. Hayes, Radio frequency field coil for NMR, U.S. Patent 4,680,548 (1987).
3. J. W. Carlson, Radiofrequency field propagation in conductive NMR samples, *J. Magn. Reson.* **78,** 563–573 (1988).
4. J. Tropp, The theory of an arbitrarily perturbed bird-cage resonator, and a simple method for restoring it to full symmetry, *J. Magn. Reson.* **95,** 235–243 (1991).
5. C. M. Collins, S. Li, Q. X. Yang, and M. B. Smith, A method for accurate calculation of B_1 fields in three dimensions. Effects of shield geometry on field strength and homogeneity in the birdcage coil, *J. Magn. Reson.* **125,** 233–241 (1997).
6. J. M. Jin and J. Chen, On the SAR and field inhomogeneity of birdcage coils loaded with the human head, *Magn. Reson. Med.* **38,** 953–963 (1997).
7. C. P. Poole, "Electron Spin Resonance, a Comprehensive Treatise on Experimental Techniques," Interscience, New York (1967).
8. M. C. Leifer, Theory of the quadrature elliptic birdcage coil, *Magn. Reson. Med.* **38,** 767–732 (1997).
9. "EMAS 4," Ansoft, Pittsburgh, PA; "Opera," Vector Fields, Aurora, IL, or Oxford, UK.
10. W. U. Roffmann, S. Crozier, K. Luescher, and D. M. Doddrell, Small birdcage resonators for high-field NMR microscopy, *J. Magn. Reson. B* **111,** 174–177 (1996).
11. F. D. Doty, Probe design and construction, *in* "Encyclopedia of NMR," Vol. 6, Wiley, New York (1996).
12. L. F. Fuks and W. A. Anderson, Perturbation method for finding the RF field on an NMR probe, poster presented at Experimental NMR Conference, Orlando (1997).

13. A. Macovski, Noise in MRI, *Magn. Reson. Med.* **36,** 494–497 (1996).
14. J. T. Vaughan, H. P. Hetherington, J. O. Otu, J. W. Pan, and G. M. Pohost, High frequency volume coils for clinical NMR imaging and spectroscopy, *Magn. Reson. Med.* **32,** 206–218 (1994).
15. S. Crozier, K. Luescher, L. K. Forbes, and D. M. Doddrell, Optimized small-bore, high-pass resonator designs, *J. Magn. Reson. B* **109,** 1–11 (1995).
16. F. D. Doty, G. Entzminger, and Y. A. Yang, Magnetism in HR NMR probe design. I. General methods, *Concepts Magn. Reson.* **10,** 133–156 (1998).
17. F. D. Doty, Optimization of MRI gradient coils *in* "Spatially Resolved Magnetic Resonance" (P. Blumler, B. Blumich, R. E. Botto, and E. Fukushima, Eds.), Wiley–VCH, Weinheim (1998).
18. F. D. Doty, T. J. Connick, X. Z. Ni, and M. N. Clingan, Noise in high power, high frequency double tuned probes, *J. Magn. Reson.* **77,** 536–549 (1988).
19. J. S. Tropp, Method of correcting an asymmetry in an NMR radio frequency coil and an improved radio frequency coil having N-fold symmetry and reduced eddy current, U.S. Patent 5,196,797 (1993).
20. J. S. Tropp, Mutual inductance in the birdcage resonator, *J. Magn. Reson.* **126,** 9–17 (1997).
21. ARRL Radio Designer 1.5, formerly Compact Software Inc., Patterson NJ, recently acquired by Ansoft, Pittsburgh, PA.
22. C. L. Chin, C. M. Collins, S. Li, B. J. Dardzinski, M. B. Smith, BirdcagBuilder V1.0, Copyright Center for NMR Research, Department of Radiology, Penn State Univ. College of Medicine, Hershey, PA (1998).
23. C. E. Hayes, Birdcage and other high homogeneity RF coils for MR, *in* "Encyclopedia of NMR," Vol. 6, Wiley, New York (1996).
24. C. L. Chin, S. Li, C. M. Collins, and M. B. Smith, Mutual inductance calculations between end-ring segments for elliptical birdcage coils, *Magn. Reson. Med.* **37,** 600–608 (1997).
25. J. R. Fitzsimmons, B. L. Beck, and H. R. Brooker, Double resonant quadrature birdcage, *Magn. Reson. Med.* **30,** 107–114 (1993).
26. L. L. Wald, L. Carvajal, S. E. Moyher, S. J. Nelso , P. E. Gran , A. J. Barkovich, and D. B. Vigneron, Phased array detectors and an automated intensity-correction algorithm for high-resolution MRI of the human brain, *Magn. Reson. Med.* **34,** 433–439 (1995).
27. O. Ocali and E. Atalar, Ultimate intrinsic signal-to-noise ratio in MRI, *Magn. Reson. Med.* **39,** 462–473 (1998).
28. F. D. Doty, Low inductance transverse Litz foil coils, patents pending, PCT No. WO 97/26560 (1997).